energies

MDPI

Article

A Dual-Stator Winding Induction Generator Based Wind-Turbine Controlled via Super-Twisting Sliding Mode

Juan I. Talpone [1,2], Paul F. Puleston [2], Marcelo G. Cendoya [2,*] and José. A. Barrado-Rodrigo [3]

1 CIDEI, Instituto Tecnológico de Buenos Aires (ITBA), C1106ACD Buenos Aires, Argentina; jtalpone@itba.edu.ar
2 Instituto LEICI, Universidad Nacional de La Plata (UNLP)/CONICET, 1900 La Plata, Argentina; puleston@ing.unlp.edu.ar
3 GAEI, DEEEA-ETSE, Universitat Rovira i Virgili (URV), 43007 Tarragona, Spain; joseantonio.barrado@urv.cat
* Correspondence: cendoya@ing.unlp.edu.ar; Tel.: +54-022-1425-9306

Received: 28 September 2019; Accepted: 3 November 2019; Published: 25 November 2019

Abstract: The dual-stator winding induction generator (DWIG) is a promising electrical machine for wind energy conversion systems, especially in the low/mid power range. Based on previous successful results utilising feed forward control, in this article, a super-twisting (ST) sliding mode improved control set-up is developed to maximise power extraction during low wind regimes. To accomplish this objective, via constant volts/hertz implementation, a ST controller was designed to command the DWIG control winding, such that the tip-speed ratio is robustly maintained at its optimal value. The proposed super-twisting control set-up was experimentally assessed to analyse its performance and to verify its efficiency in an actual generation test bench. The results showed a fast convergence to maximum power operation, avoiding chattering and offsets due to model uncertainties.

Keywords: wind energy; control; dual-stator winding induction generator; second order sliding mode

1. Introduction

Variable speed wind turbines have high efficiency in a wide range of wind speeds. This kind of wind energy conversion system (WECS) can use different types of electric generators and control techniques. In variable speed operation, when wind turbines are connected to an electrical network, it is necessary to include some frequency conversion stages [1,2]. In practice, there are two widespread power topologies: (a) a power converter connected between the stator winding of the generator and the grid, and (b) a power converter connected between the wound rotor of the generator and the electrical network.

The wind power systems of the first group usually use brushless machines, such as the squirrel cage induction generator (SCIG) or the permanent magnet synchronous generator (PMSG); and they require a converter of the same power as the generator (full power converter). While for the second group, usually a doubly fed induction generator (DFIG) is used. In this asynchronous machine, the stator is connected directly to the grid, and the rotor is fed through a bidirectional converter. This system has the advantage that it requires a converter which must deal with only a fraction of the total generator power (fractional power converter). On the downside, the wound rotor presents maintenance problems with the rings and brushes.

The dual-stator winding induction generator (DWIG) with brushless rotor seems to be a good option that combines the advantages of the two groups of generators mentioned above, since it is a very robust and reliable electrical machine, in which one of the stator windings is fed via a fractional

controlled power converter, while the other winding can be directly connected to the grid. There are some options of induction generator with two sets of stator windings and brushless rotor that can be used in variable speed wind turbine systems [3]. In all these options, the two sets of stator windings are electrically isolated, in some cases with different pole numbers and various rotor configurations. Thus, in practice, the DWIG types can be

Case (I) a dual-stator induction machine having the two sets of three-phase windings, with the same pole number, but with a spatial shift of 30 electrical degrees. The rotor is a standard squirrel cage.

Case (II) a dual-stator induction machine having the two sets of stator windings with dissimilar pole numbers and the rotor is a nested-loop arrangement. One of the stator windings is directly connected to the grid (called power winding-PW), and the other stator winding (called control winding-CW) is connected to the grid via a fractionally rated frequency converter.

Case (III) a dual-stator induction machine having the two sets of three-phase windings with different numbers of poles in a 1:3 ratio. This configuration is usually chosen from the viewpoint of better magnetic utilization and to eliminate magnetic coupling between windings [4]. In this case, the rotor is a standard squirrel cage rotor.

Regarding the control strategies of variable speed wind energy conversion systems based on a dual-stator winding induction generator (WECS-DWIG), in [5], various approaches for DWIG with similar pole number are compared. The analysed control strategies are instantaneous slip frequency control (ISFC), field oriented control (FOC), voltage oriented control (VOC) and direct power control (DPC); whereas, in [6], a first order sliding mode (FOSM) controller for this type of induction generator is described.

There are some works about DWIG with dissimilar pole numbers, and a nested loop rotor, applied in variable speed wind turbines. Usually in this wind generator, the PW is connected directly to the grid, and CW is supplied via a bidirectional power converter. This topology is called a brushless doubly fed induction generator (BDFIG). In [7], a direct torque control (DTC) strategy for this BDFIG system is shown. Likewise, Ref. [8] developed a field oriented control (FOC), and [9] developed FOSM control strategies.

Additionally, for the third case of DWIG (dissimilar pole numbers and squirrel cage rotor), a high-performance control of a DC generating system was proposed by [10]. That paper shows two topological structures, using series (or parallel) connected AC-DC pulse width modulation rectifiers between each stator winding and the DC bus. A wind turbine system with a stator winding of DWIG connected directly to the grid was presented in [11]. Up to a certain value of wind speed, the induction generator works only with CW and its power converter. Under these conditions, a feed forward scalar control is applied to the generator. For higher wind speed, the PW is connected directly to the grid. In this zone of operation, with both stator windings working together, the wind turbine turns at quasi-constant speed. As a complementary work, Ref. [12] studied the capability of this DWIG to grid disturbances.

Encouraged by the good results that the authors have obtained in [11] using a feed forward action to control the WECS-DWIG, as a next step in that research, this paper proposes an improved control set-up based on a sliding mode (SM) control strategy [13]. Specifically, a controller that combines a feed forward action with a feedback second order sliding mode (SOSM) super-twisting (ST) algorithm [14,15]. This technique has been chosen because SOSM based controllers have shown numerous advantages to control nonlinear systems under heavy disturbances [16–22], in particular WECS [23–28]. Some of these proven advantages are: robustness to several bounded parameter variations, uncertainties and external disturbances; reduction of mechanical stresses and chattering, thanks to applying the discontinue control action at the output second-derivative level; and control laws of relatively low computational cost.

This paper is organized as follows. In Section 2, the DWIG based WECS under study is described, its operation zones are explained and a dynamic model of the system is presented. In Section 3, the ST

control set-up to robustly achieve MPPT is designed. In Section 4, experimental results are shown and analysed. Finally, in Section 5, the work's conclusions and future research lines are discussed.

2. DWIG Based Wind Energy Conversion System

2.1. System Description

The wind energy conversion topology under study is shown in Figure 1. A three-bladed horizontal axis wind turbine drives the rotor of the DWIG by means of a multiplier gearbox (GB), so that the rotational speed of the generator remains in a useful operating range. As mentioned, the DWIG has a squirrel cage rotor and two stator windings of different pole numbers, the power winding PW and the control winding CW. The PW can be connected directly to the network via a power contactor, commanded by an upper level supervisory system depending on the operation zone. There is a capacitor bank in parallel with this winding to improve the power factor. As for the CW, it is indirectly linked to the grid by means of two three-phase inverters arranged in back to back connection sharing a common DC link. With this electronic conversion chain, the CW can be fed with a frequency and voltage different from that of the grid. The supply voltage of the CW is varied, through sinusoidal PWM modulation, accompanying the variation of the frequency following a constant V/f ratio. In this way, the air gap rotating magnetic field produced by the CW is maintained at its rated value throughout the operating range of the system. The inverter that connects the CW to the grid has a control loop associated with it, whose objective is to keep the DC bus voltage constant.

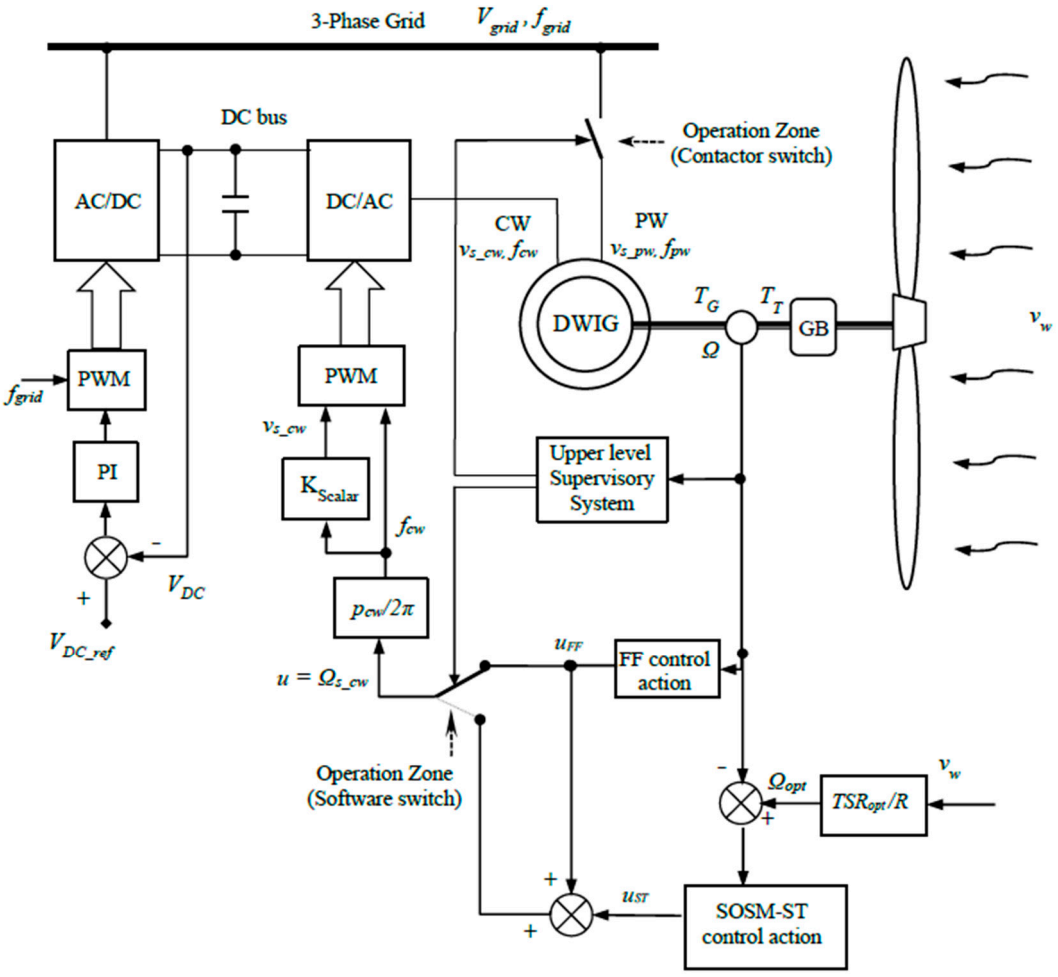

Figure 1. Structure of the wind energy conversion system based on a dual-stator winding induction generator (DWIG).

2.2. Wind Turbine Model

The wind turbine extracts a fraction of the wind power, depending on its aerodynamic efficiency given by the power coefficient C_p. Then, the turbine power can be expressed as ([27])

$$P_T(\Omega, v_w) = C_p(TSR)P_{wind}(v_w) = C_p(TSR)\frac{1}{2}\rho\pi R^2 v_w^3 \quad (1)$$

where Ω is the mechanical rotational speed, v_w is the wind speed, P_{wind} is the kinetic power of the wind, ρ is the air density and R is the blades' length. Coefficient $Cp(TSR)$ depends on the topology and dimensions of the blades and it is, in fact, a nonlinear function of the tip speed ratio:

$$TSR = \frac{R\Omega}{v_w} \quad (2)$$

The $Cp(TSR)$ of the horizontal axis wind turbine considered in this paper is depicted in Figure 2 (referred to the generator side). It has been assumed fixed blade pitch angle given that, in the operation zones under study, it is fixed at its optimal value of maximum power extraction (operation when the DWIG rated power is reached is beyond the scope of this work. In that situation, the supervisory system should turn into variable pitch operation to restrain the power extraction and to protect the generator).

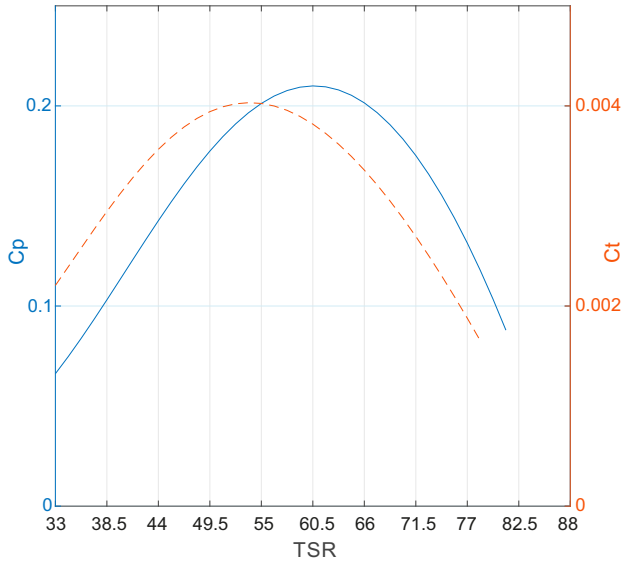

Figure 2. Wind turbine power (blue) and torque coefficients (dashed-red) versus tip speed ratio (both referred to the generator side).

In Figure 2 it can be appreciated that $Cp(TSR)$ presents a unique maximum at $TSR_{opt} = 60.5$. Therefore, the objective of maximum power point tracking or maximum wind power extraction would be accomplished by tracking a variable optimum speed reference Ω_{opt}, designed to maintain $TRS = TSR_{opt}$. From Equation (2):

$$\Omega_{opt} = \frac{TSR_{opt}}{R} v_w \quad (3)$$

As for the turbine torque, it is given by

$$T_T(\Omega, v_w) = \frac{P_T(\Omega, v_w)}{\Omega} = C_T(TSR)\frac{1}{2}\rho\pi R^3 v_w^2 \quad (4)$$

where $C_T(TSR) = \frac{C_P(TSR)}{TSR}$ is the turbine torque coefficient (see Figure 2). Turbine torque curves as a function of the rotation speed (referred to the generator side), for different wind speeds, can be appreciated in Figure 3 in the blue-dashed line.

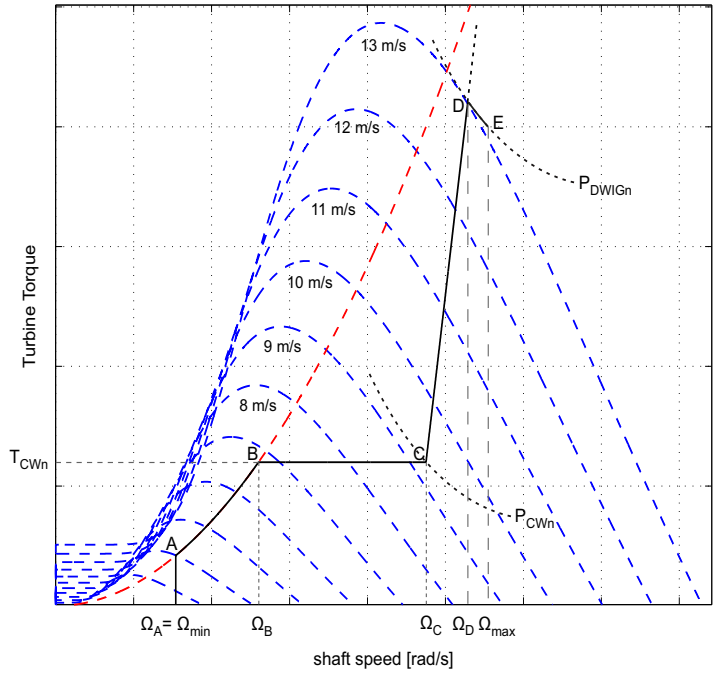

Figure 3. Operating zones of the wind energy conversion system based on a DWIG.

Then, from Equation (4) and considering TSR_{opt} , the expression of the optimal torque can be obtained:

$$T_{opt}(\Omega) = \frac{C_T\left(TSR_{opt}\right)\frac{1}{2}\rho\pi R^5}{{TSR_{opt}}^2}\Omega^2 = K_{opt}\Omega^2 \quad (5)$$

that is, the expression of the T_T corresponding to the maximum power point tracking (MPPT) as a function of the rotational speed Ω (depicted in the red-dashed line in Figure 3).

To conclude this subsection, it is worth mentioning that, in this paper, the high-speed side of the gear box has been chosen to work with, so the turbine variables in the article are referring to the generator side through the transmission ratio, GB.

2.3. WECS-DWIG System Operation Zones

In the complete range of operation, the DWIG based WECS's functioning modes are associated to four different zones which can be illustrated in the shaft speed–torque (see black line in Figure 3). From the measurement of Ω, an upper level supervisory system must identify the current zone and, consequently, set the pertinent operation mode.

This paper focuses on improving the conversion efficiency in the zone corresponding to low wind regimes, to ensure the best use of the scarce resource. However, to frame the design in a comprehensive context, in this subsection a succinct outline of all four operations zones is provided (a detailed description and analysis can be found in [11]).

- *Operation in Zone AB*. During low wind speed periods the objective is to maximize the energy extraction from the wind. Thus, a maximum power point tracking (MPPT) strategy is established for the CW whereas, in this operation zone, the PW remains disconnected from the grid (points of maximum wind power generation are depicted in red-dashed line in Figure 3). This zone starts at

point A (at minimum speed Ω_{min}) and ends at point B (corresponding speed Ω_B), where the rated current of the control winding is attained and its nominal torque is reached.

- *Operation in Zone BC*: From point B on, if the wind speed increases, the DWIG's control system abandons the MPPT and changes the control objective to CW current regulation $i_{s\_cw} = i_{s\_cw\_RATED}$ (equivalently, constant torque), to prevent generator damages. When the shaft speed reaches Ω_C the control winding is operating at its rated power P_{CWn} (point C).
- *Operation in Zone CD*: corresponds to operation during high wind speed regimes. From point C, if the wind speed keep increasing, the CW would not be able to process the full amount of the wind power, thus, the supervisory system maintains current regulation for the CW, but also connects the PW directly to the grid to extract the wind energy surplus. When the shaft speed reaches Ω_D, the DWIG is working at point D, delivering the generator rated power P_{DWIGn}. This power is the maximum that can be obtained with both windings, CW and PW, in operation.
- *Operation beyond point D*: an appropriate mechanism to limit DWIG power and a maximum speed Ω_{max} (for instance, a variable pitch control system) is needed to avoid WECS damage or even destruction.

2.4. Wind Energy Conversion System Dynamics

- *DWIG Electrical Dynamics*

The DWIG has a squirrel cage rotor, the latter designed to be magnetically coupled to both the control and power windings of the stator, respectively. Regarding the stator windings, the number of CW pole pairs is three times the number of PW pole pairs, to eliminate the magnetic coupling between both windings, separating their influence on the generator torque [4]. In the experimental equipment under study, the pair of poles are $p_{cw} = 3$ and $p_{pw} = 1$, respectively (see windings details in Figure 4).

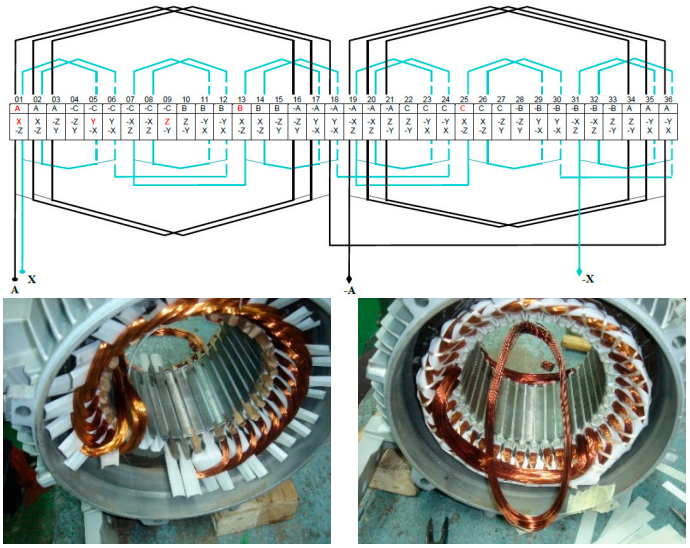

Figure 4. Schematic and images of the DWIG's control and power stator windings. Control winding (CW; 1/3 of maximum power): XYZ. 6 poles, 36 coils of 28 turns. Power winding (PW; 2/3 of maximum power): ABC. 2 poles, 18 coils of 36 turns.

The aforementioned decoupling effect makes the DWIG work as two separate induction machines that share the same mechanical shaft. Consequently, the dynamic electrical model of the DWIG in the

time domain, considering a *dq* synchronous reference frame (after applying the Park transformation to the model expressed in phase variables), can be written as ([11])

$$\begin{cases} v_{qds\_pw} = R_{s\_pw} i_{qds\_pw} + p_{pw} \Omega_{s\_pw} \lambda_{dqs\_pw} + \frac{d\lambda_{qds\_pw}}{dt} \\ v_{qdr\_pw} = 0 = R_{r\_pw} i_{qdr\_pw} + p_{pw} \left(\Omega_{s\_pw} - \Omega \right) \lambda_{dqr\_pw} + \frac{d\lambda_{qdr\_pw}}{dt} \end{cases} \tag{6}$$

$$\begin{cases} v_{qds\_cw} = R_{s\_cw} i_{qds\_cw} + p_{cw} \Omega_{s\_cw} \lambda_{dqs\_cw} + \frac{d\lambda_{qds\_cw}}{dt} \\ v_{qdr\_cw} = 0 = R_{r\_cw} i_{qdr\_cw} + p_{cw} (\Omega_{s\_cw} - \Omega) \lambda_{dqr\_cw} + \frac{d\lambda_{qdr\_cw}}{dt} \end{cases} \tag{7}$$

In Equations (6) and (7) R are winding resistances, where subscripts s and r refer to the stator and rotor side, while *pw* and *cw* refer to the PW and the CW. p are the pole pairs and λ is the magnetic flux. Ω is the shaft speed and Ω_s is the mechanical synchronous speed, defined for each winding as

$$\Omega_{s\_pw} = \frac{2\pi f_{pw}}{p_{pw}}, \; \Omega_{s\_cw} = \frac{2\pi f_{cw}}{p_{cw}} \tag{8}$$

where f_{pw} and f_{cw} are the electrical frequency of the power supplies that feed each stator winding.

The flux linkage equations are

$$\begin{cases} \lambda_{qds\_n} = \left(L_{ls\_n} + \frac{3}{2} L_{ms\_n} \right) i_{qds\_n} + \frac{3}{2} L_{ms\_n} i_{qdr\_n} \\ \lambda_{qdr\_n} = \left(L_{lr\_n} + \frac{3}{2} L_{mr\_n} \right) i_{qdr\_n} + \frac{3}{2} L_{ms\_n} i_{qds\_n} \end{cases} \tag{9}$$

In Equation (9), L_l are leakage inductances and L_m mutual inductances, where the sub-index "n" stands for "*pw*" or "*cw*" depending on the stator winding.

The total electromagnetic torque of the DWIG, is given by

$$\begin{aligned} T_G = \; & T_{Gpw} + T_{Gcw} \\ & = \tfrac{3}{2} p_{pw} L_{ms\_pw} \left(i_{qs\_pw} i_{dr\_pw} - i_{ds\_pw} i_{qr\_pw} \right) + \tfrac{3}{2} p_{cw} L_{ms\_cw} \left(i_{qs\_cw} i_{dr\_cw} - i_{ds\_cw} i_{qr\_cw} \right) \end{aligned} \tag{10}$$

- *WECS Mechanical Dynamics*

The mechanical dynamics of the WECS-DWIG is determined by Newton's law:

$$J \frac{d\Omega}{dt} = T_T - T_G - T_r \tag{11}$$

where T_r is the friction torque and J is the combined inertia of the whole rotating parts.

3. WECS-DWIG Super-Twisting Based Proposed Control

As it was stated, the super-twisting based control set-up designed in this paper focuses on optimizing the WECS operation during low wind speeds regimes, when maximum power extraction is required (Zone AB in Figure 3). In this zone, only the DWIG's control winding is functioning. Recalling (5), to fulfil the control objective of MPPT, the system must operate at $T_{opt}(\Omega)$, which can be attained by tracking the optimal speed reference, given by $\Omega_{opt} = \frac{TSR_{opt}}{R} v_w$.

The control past point B is treated in detail in [11] and it is beyond the scope of this paper. In particular, the control winding in Zone BC and Zone CD is controlled for power limitation (consequently, constant current control), which is successfully implemented through a simple feed forward (FF) action. Whereas, the power winding is only operative in Zone CD, where it is directly connected to the grid [11]. Above the rated wind speed (i.e., when the maximum power of the DWIG is reached), an external power limiting mechanism must exist (possibly involving active or passive modification of the aerodynamic characteristics of the blades).

3.1. WECS Model for the Control Design

A reduced order model can be used for the design of the proposed controller. In WECS, the electrical dynamics are considerably faster than the mechanical ones, then a practical assumption for the design of the controller is to neglect the electrical dynamics. Under this consideration, the torque of the DWIG in zones AB and BC becomes ([29])

$$T_G = T_{Gcw} = 3\frac{p_{cw}R_{r\_cw}}{s_{cw}(2\pi f_{cw})}\frac{v_{s\_cw}^2}{\left[\left(R_{s\_cw}+\frac{R_{r\_cw}}{s_{cw}}\right)^2+(2\pi f_{cw})^2(L_{ls\_cw}+L_{lr\_cw})^2\right]} \tag{12}$$

where s_{cw} is the CW slip relative to Ω_{s_cw}, defined as

$$s_{cw} = \frac{\Omega - \Omega_{s\_cw}}{\Omega_{s\_cw}} \tag{13}$$

If $s_{cw} << 1$, then Equation (12) can be approximated by the linear expression [29]:

$$T_G = 3\frac{p_{cw}^2}{R_{r\_cw}}\left(\frac{v_{s\_cw}}{2\pi f_{cw}}\right)^2(\Omega - \Omega_{s\_cw}) \tag{14}$$

Moreover, the DWIG is commanded using a scalar technique, i.e., the CW is fed with sinusoidal voltages whose frequency f_{cw} is varied to maintain a constant $\frac{v_{s\_cw}}{f_{cw}}$ ratio, then Equation (14) can be expressed as

$$T_G = K_T(\Omega - \Omega_{s\_cw}) \tag{15}$$

The numerical value of the torque constant K_T in Equation (15) can be experimentally obtained or computed from the DWIG parameters using Equation (14).

Finally, substituting Equation (15) into the equation of the dominant dynamics Equation (11) and neglecting the friction, it yields the following reduced order model for the control design:

$$\dot{x} = f(x, v_w) + gu \tag{16}$$

$$f(x, v_w) = \left(\frac{T_T(x, v_w)}{J} - \frac{K_T}{J}x\right) \text{ and } g = \frac{K_T}{J}$$

with the state variable $x = \Omega$ and the control input $u = \Omega_{s\_cw}$. Note that it would have been possible to include in Equation (16) a term to model the nominal torque friction, leaving a reduced uncertainty for T_r. However, it was preferred to consider the latter completely unknown for the design. In this way, the experimental results obtained with the *ST* control set-up will better prove the effectiveness and robustness of the proposed controller in real operation, even facing such assumed unknown friction together with the other existing uncertainties/disturbances.

3.2. Super-Twisting Based Control Set-Up Design

The proposed *ST* control set-up comprises two control terms:

$$u = u_{FF} + u_{ST} \tag{17}$$

The first one is a feed forward (FF) control action, in charge of steering the system to the neighborhood of the desired $T_{opt}(\Omega)$ zone. The second one is a SOSM ST control action, responsible for accurately performing MPPT during scarce wind regimes (i.e., Zone AB), even in the presence of disturbances and uncertainties with respect to the nominal WECS-DWIG model.

3.2.1. Feed-Forward Control Term

Firstly, for the design of the feed forward control action, the steady state torque balance of the system is obtained from Equation (11), i.e., $T_T = T_G + T_r$. Then, assuming that the optimal torque is attained, $T_T = T_{opt}(\Omega)$, under ideal operation (undisturbed system and neglecting friction) the torque balance gives

$$T_{opt}(\Omega) = K_{opt}\Omega^2 = T_G = K_T(\Omega - \Omega_{s\_cw}) \tag{18}$$

and the expression of the proposed Feed Forward action results in

$$\Omega_{s\_cw}\big|_{T_T = T_{opt}} = u_{FF} = \Omega - \frac{K_{opt}}{K_T}\Omega^2 \tag{19}$$

Note that, even though u_{FF} cannot accurately deal with the uncertainties of the real WECS, this feed forward approach has proven to be successful to lead the system to the vicinity of T_{opt} [11].

3.2.2. SOSM Super-Twisting Control Term

During low wind regimes, the resource is scarce, so it is of paramount importance to extract as much energy from the wind as possible. As previously said, the proposed feed forward action is an effective technique to guide the system to the proximity of T_{opt}, although to attain a highly precise MPPT in a real generation system, the incorporation of a robust feedback control action is essential.

To this end, a SOSM technique has been selected to implement such robust feedback control term for the dual-stator winding induction generator based WECS under consideration. SOSM has demonstrated to be a suitable design tool applicable to several WECS topologies based on conventional induction or synchronous generators.

To track the optimum shaft speed in Equation (3), the following smooth sliding variable σ can be defined:

$$\sigma = \Omega - \Omega_{opt} = \Omega - \frac{TSR_{opt}}{R}v_w \tag{20}$$

which is of relative degree (RD) 1 with respect to the input u in Equation (16).

Then, a super-twisting algorithm is selected to synthetize the SOSM control term u_{ST}. In addition to be suitable for σ of RD 1, this robust control SOSM algorithm also avoids direct discontinuous control action, reducing mechanical stresses and diminishing chattering. Plus, it does not require measurement of the sliding variable time derivative $\dot{\sigma}$. The selected ST control term is given by ([30])

$$u_{ST} = -\beta|\sigma|^{\frac{1}{2}}sign(\sigma) - \alpha\int_0^t sign(\sigma(\tau))d\tau \tag{21}$$

where β and α are the control gains.

With an appropriate tuning of those gains, the ST guarantees the zeroing of σ and $\dot{\sigma}$ in finite time, which implies robust MPPT operating at $\Omega = \Omega_{opt}(t)$ for variable wind speeds.

For the design of such gains, it is required to compute and obtain bounds for the second time-derivative of the sliding variable. The first step is to substitute Equation (16) into Equation (20) and to differentiate σ twice:

$$\ddot{\sigma} = \left[\dot{f}(\Omega, v_w) + g\dot{u}\right] - \ddot{\Omega}_{opt} = \left[\dot{f}(\Omega, v_w) - \ddot{\Omega}_{opt}\right] + \frac{K_T}{J}\dot{u} \tag{22}$$

Using Equation (17), it can be written in affine form with respect to $\dot{u}_{ST}$ as

$$\ddot{\sigma} = \left[\dot{f}(\Omega, v_w) - \ddot{\Omega}_{opt} + \frac{K_T}{J}\dot{u}_{FF}\right] + \frac{K_T}{J}\dot{u}_{ST} = \varphi + \gamma\dot{u}_{ST} \tag{23}$$

where functions φ and γ are bounded by positive constants Φ, Γ_m, and Γ_M as

$$-\Phi \leq \varphi \leq \Phi \text{ and } \Gamma_m \leq \gamma \leq \Gamma_M \tag{24}$$

including, in the bounding process, the uncertainties and disturbances to be rejected.

Then, the *ST* control gains must be tuned to fulfil the following conditions:

$$\alpha > \frac{\Phi}{\Gamma_m} \text{ and } \beta^2 \geq \frac{4\Phi}{\Gamma_m^2} \frac{\Gamma_M(\alpha+\Phi)}{\Gamma_m(\alpha-\Phi)} \tag{25}$$

To obtain the bounds for the WECS-DWIG under study, an essentially practical procedure has been followed:

- Firstly, primary bounds were obtained through systematic simulation tests, complemented with a detailed analysis of the actual system topology and limitations. In this framework, simulations were run to thoroughly assess the behavior of functions $\varphi = \dot{f}(\Omega, v_w) - \ddot{\Omega}_{opt} + \frac{K_T}{J}\dot{u}_{FF}$, and $\gamma = \frac{K_T}{J}$ under the effect of several wind profiles, disturbances, and model uncertainties, covering the operation range of Zone AB.
- To conclude the design, the main phase, i.e., the experimental tuning phase, was performed. The ST-SOSM controller was implemented in the testing workbench. Based on the previous bounds, different sets of preliminary control gains β and α fulfilling Equation (25) were programmed. Then, progressive refinement of the control gains was undertaken, conducting iterative laboratory tests, and gains β and α were chosen, prioritising the chattering reduction in the definitive selection. The resulting gains for the *ST* implementation are

$$\alpha = 0.038 \text{ and } \beta = 0.12$$

It is worth noting that these two gains are computed off-line during the tuning procedure, so on-line operation of the *ST* control term is rather simple.

4. Experimental Results

This section presents the experimental results of the proposed ST control set-up for the DWIG based WECS. The features of the controller aiming to MPPT are examined through two sets of experiments. Case Study 1 shows the performance of the controlled system under a realistic variable wind speed profile, while in Case Study 2, a stepped wind profile is considered, to better analyse and compare the transient response of the controlled system.

Before presenting the results, a brief description of the equipment used in the tests, whose picture is shown in Figure 5, is given in the next few paragraphs.

Figure 5. Experimental set-up.

The experimental set-up is made up of two fundamental subsystems: the DWIG generation system module and the wind turbine emulator module.

- *DWIG Generation System Module*

The generation system module consists of a DWIG prototype, designed and constructed in the URV laboratory, with a power electronic conversion chain and its associated control system, to feed the stator CW with variable voltage and frequency, keeping a constant V/f ratio.

The DWIG prototype's most significant technical data—rated power: 5.5 kW (CW: 1.8 kW and PW: 3.7 kW), rated synchronous speed: 314 rad/s (3000 rpm), rated torque: 18 Nm, rated voltages for both PW and CW: 400 V_{RMS} (wye connection), rated frequency: 50 Hz, rated current: CW = 2.6 A/phase and PW = 5.3 A/phase. The electrical parameters of the windings—PW: R_{s_pw} = 2.9 Ω, R_{r_pw} = 1.2 Ω, L_{ls_pw} = L_{lr_pw} = 9.8 mH, L_{m_pw} = 470 mH; CW: R_{s_cw} = 5.5 Ω, R_{r_cw} = 2.4 Ω, L_{ls_cw} = L_{lr_cw} = 4.6 mH, L_{m_cw} = 175 mH. Then, the numerical value of the torque constant K_T in Equation (15) is 1.105 [Nm/(rad/s)] and was experimentally obtained and verified from the DWIG parameters using Equation (14).

The CW is fed by a three-phase inverter made with a Semikron Semistack SKS-35F power module that comprises a bridge rectifier and a 1200 V, 35 A three-legged IGBT CC-CA converter that supports a 15 kHz maximum switching frequency. The three-phase inverter output voltage can be varied by means of a symmetric regular sampled sinusoidal PWM method, implemented in a Cortex® M4 120 MHz Texas Instruments Tiva C Series TM4C1294NCPDT Microcontroller, with a carrier frequency of 5 kHz and with overmodulation capability.

A Hewlett-Packard programmable DC electronic power supply (1000 V_{DCmax}, 15 kW, with bidirectional current capability), working as a constant voltage source, is connected to the inverter DC-link. The power supply behaves as a dummy load, absorbing the active power delivered by the CW. The DC-link is regulated at 600 V_{DC}, which is an adequate value so that the three-phase inverter can deliver the CW rated voltage.

- *Wind Turbine Emulator Module*

The wind turbine emulator is based on a Texas Instruments DSP F28335-TMS320 which computes the turbine torque from a programmed turbine characteristic, the measurement of the DWIG shaft speed and the desired wind speed. Such variable wind profile can be either downloaded to memory or entered via keypad. This computed torque acts as reference for the driving electric machine, a SIEMENS three-phase induction motor (model: 1LA71632AA) of 11 kW, 400 V, 50 Hz and 2 poles (3000 rpm synchronous speed), fed by a SIEMENS Micromaster MM440 frequency converter.

For these tests, a 5.6 kW three-blade horizontal axis wind turbine coupled to the DWIG trough a gearbox with a 1:11 speed ratio is emulated, with R = 2.5 m and TSR_{opt} = 60.5 (generator side).

4.1. Case Study 1: Variable Wind Speed Profile

The first series of tests was performed using a realistic wind speed profile, which is shown in Figure 6. Note that its maximum wind speed was below 7.5 m/s to ensure operation under a scarce wind regime, so the WECS-DWIG is functioning in conditions that maximum wind power extraction is of paramount importance (i.e., Zone AB with MPPT objective).

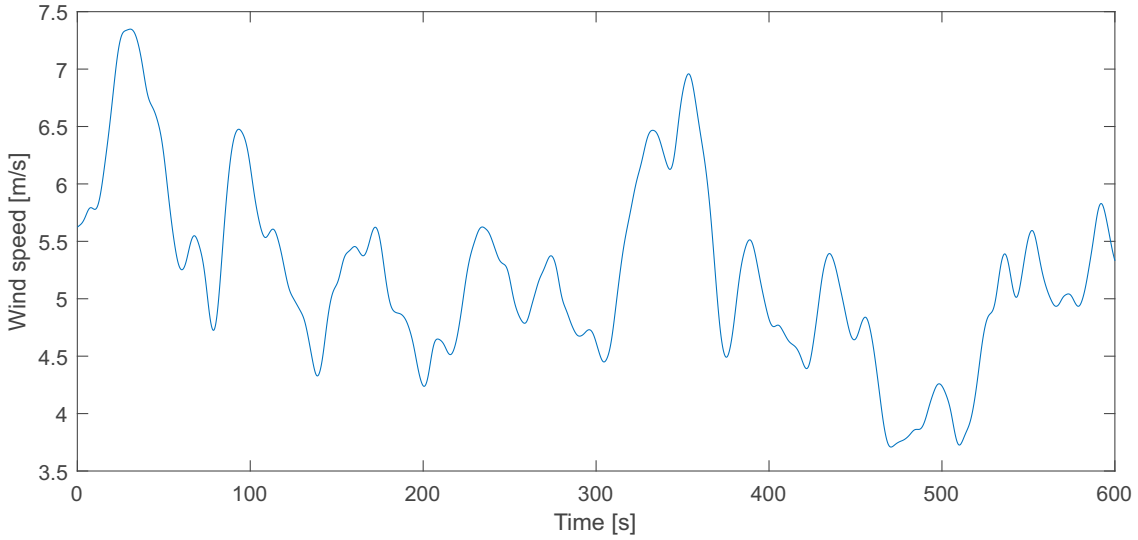

Figure 6. Variable wind speed profile.

Figure 7 shows the corresponding optimum speed Ω_{opt} in orange dashed line. That is, the temporal evolution of the reference speed for maximum power extraction in accordance with Equation (18). In addition, in blue, the real DWIG shaft speed when only the FF controller is employed is depicted [11]. It can be appreciated that the feed forward approach provides good tracking of the optimum speed. However, due to disturbances and uncertainties with respect to the real system, it is evident that a certain persistent error exists, being of particular interest to avoid it when the wind resource is scarce (in several periods, for instance around 475 s, the speed error reaches values of approximately 20%).

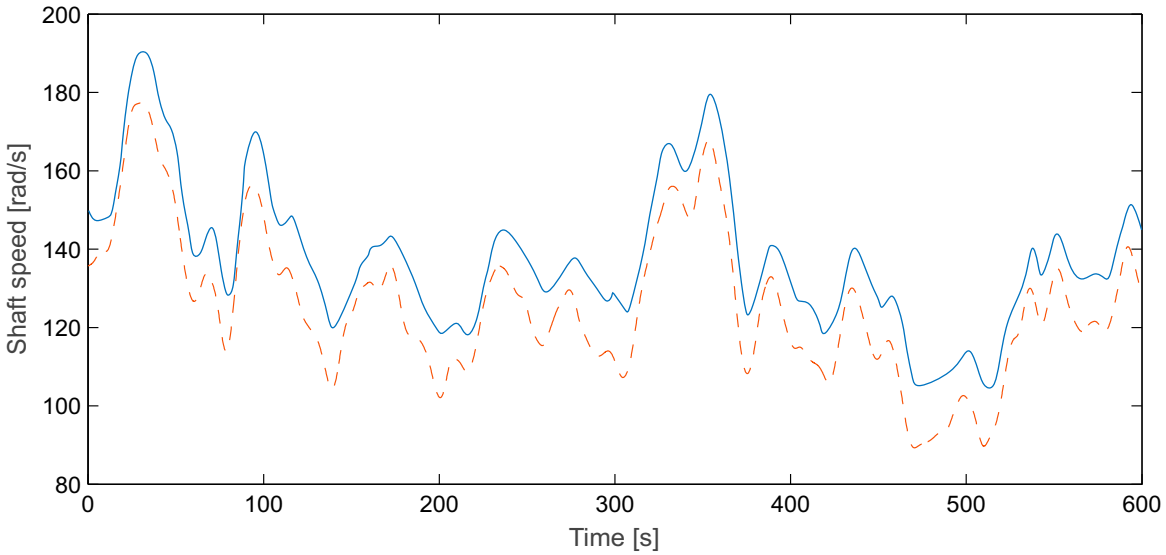

Figure 7. Optimal rotational speed reference for the variable wind profile (orange dashed line) and experimental speed tracking using only the feed forward (FF) controller (blue line).

As a counterpart, Figure 8 displays the experimental results obtained with the ST control set-up designed in Section 3.2. It can be observed that the behavior of the WECS-DWIG under the combine action of the proposed ST + FF strategy greatly improves. The shaft rotational, in practice, precisely overlaps the desired optimum speed Ω_{opt}, consequently excellent MPPT is attained. It is interesting to compare the system evolution in the DWIG speed-torque plane (Figure 9b), with the previous case, plotted in Figure 9a. It is notable how the SOSM based controller steers the system to travel almost over the optimum torque locus.

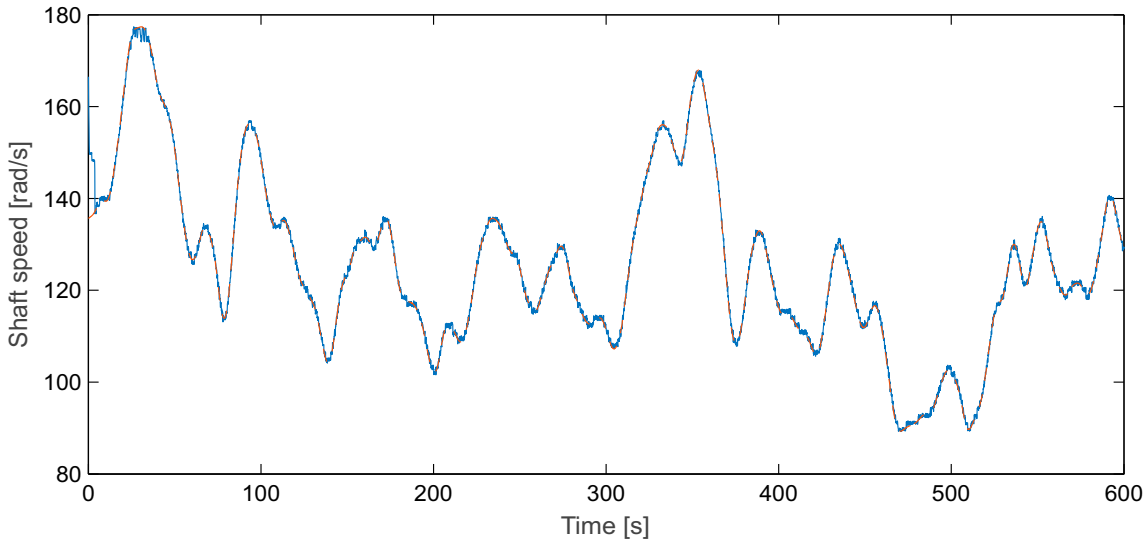

Figure 8. Optimal rotational speed reference for the random wind profile and experimental speed tracking using the proposed FF + ST (super-twisting) control set-up (overlapped).

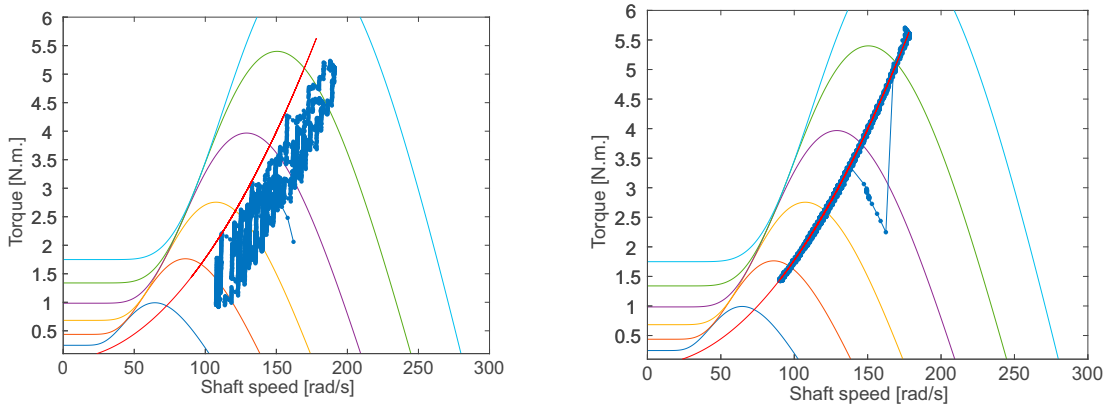

Figure 9. Evolution of the system operating points in the speed-torque plane (blue line) and optimal torque locus $T_{opt}(\Omega)$ (red parabola). (**a**) FF controller; (**b**) Proposed ST + FF control set-up.

Such reduction in the wind turbine conversion efficiency can be clearly visualised in the actual rotational speed-torque plane (see Figure 9a), where the operating points do not precisely evolve over the parabola of optimum torque $T_{opt}(\Omega)$, given by Equation (19). This, in turn, means that the power extraction is lower than the maximum available power in the wind.

Figure 10 shows the theoretical maximum power that the turbine can extract from the wind (red line), obtained from Equation (1) with $Cp(TSR_{opt})$, together with the actual power extracted by both controllers. It is clear that the proposed FF + ST controller practically allows full advantage of the wind resource (dashed blue) to be taken; whereas, using the FF controller (yellow line), some power available in the wind is wasted (e.g., about 23% around 510 s).

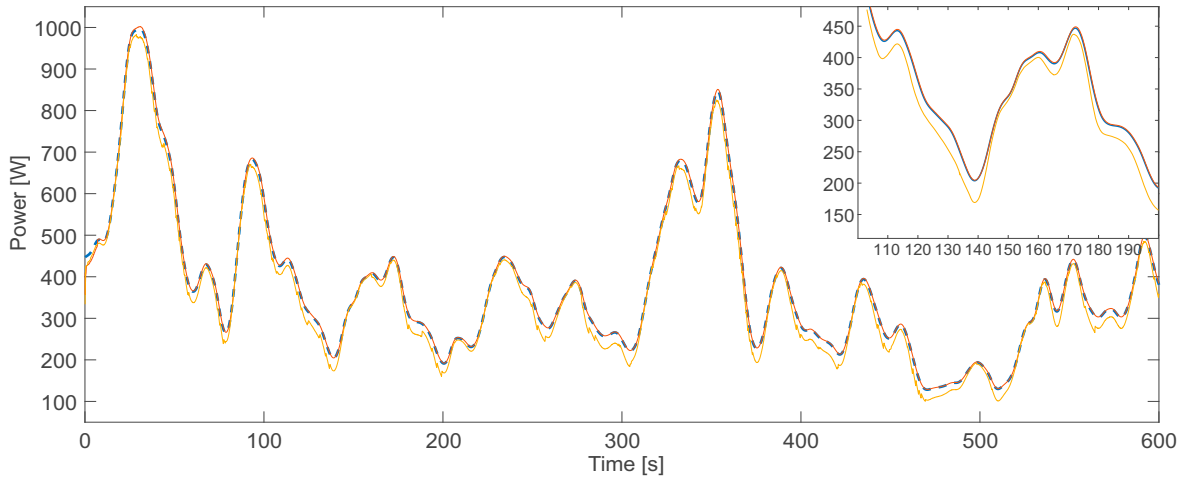

Figure 10. Maximum power the turbine can extract from the wind (red line). Actual extracted power using the FF + ST controller (dashed blue). Actual extracted power using the FF controller (yellow line).

Finally, the controllers control actions (namely, the mechanical synchronous speed of the CW, $\Omega_{s\_cw} = \frac{2\pi f_{cw}}{p_{cw}}$) are depicted in Figure 11a,b.

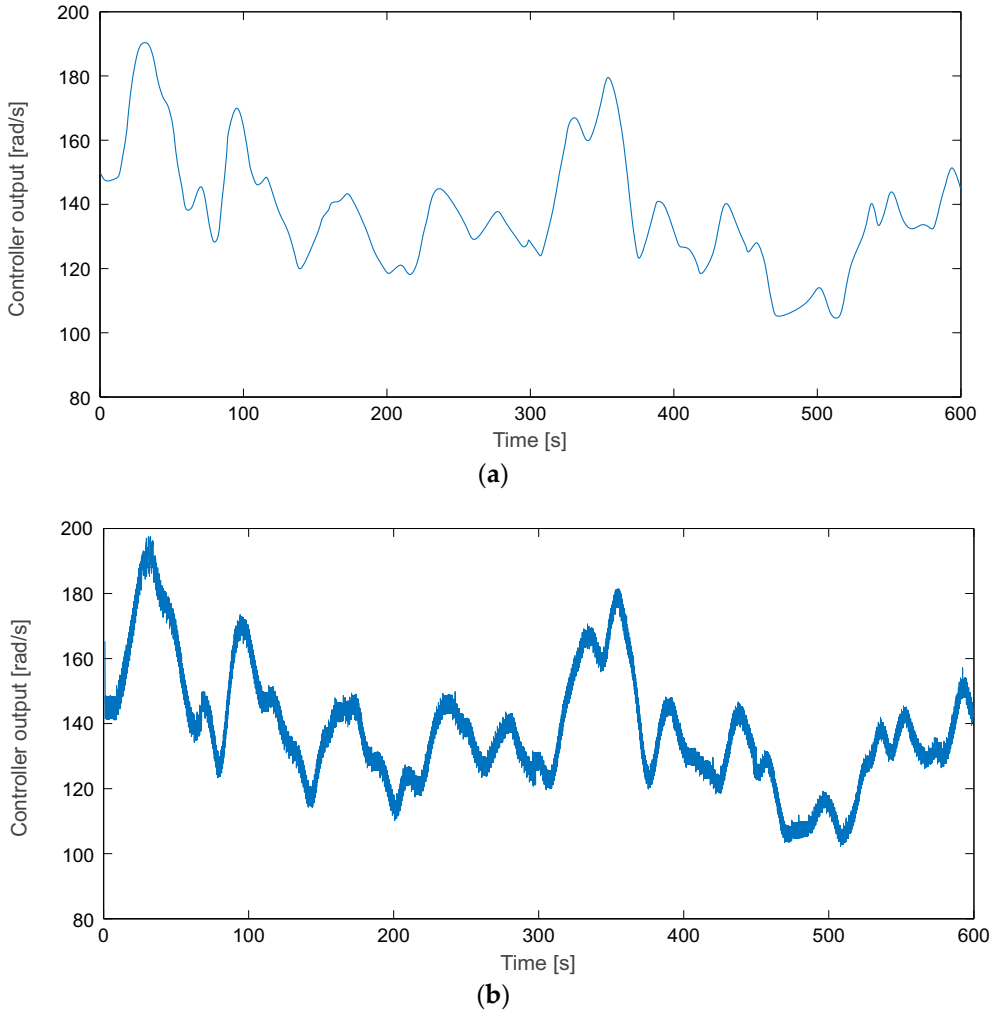

Figure 11. Control action $\Omega_{s\_cw} = \frac{2\pi f_{cw}}{p_{cw}}$ (**a**) FF controller and (**b**) FF + ST controller.

4.2. Case Study 2 Stepped Wind Profile

The second series of experimental tests is done using the stepped wind speed profile depicted in Figure 12. This is not a realistic profile, but it is of interest for the visualization of the transient and steady state responses of the controlled WECS-DWIG under study.

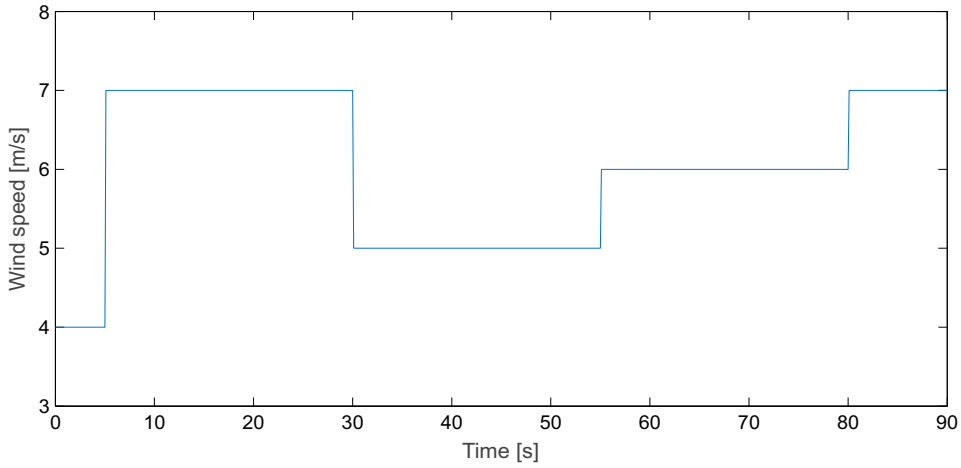

Figure 12. Stepped wind profile used in the tests.

The first experimental test corresponds to the feed forward controller on its own (blue line in Figure 13). The optimal shaft speed reference Ω_{opt} is plotted in orange dashed line. Similarly to Case Study 1, even though the FF controller proves its capability to steer the system to the neighborhood of reference Ω_{opt}, a remnant offset is clearly visible (approximately 15 rad/s in excess, corresponding to 17% at the lower speed), due to disturbances and model errors with respect to the real WECS-DWIG. Besides, in the zoomed view it can also be observed a noticeable settling-time (approximately 2 s) until steady state is reached.

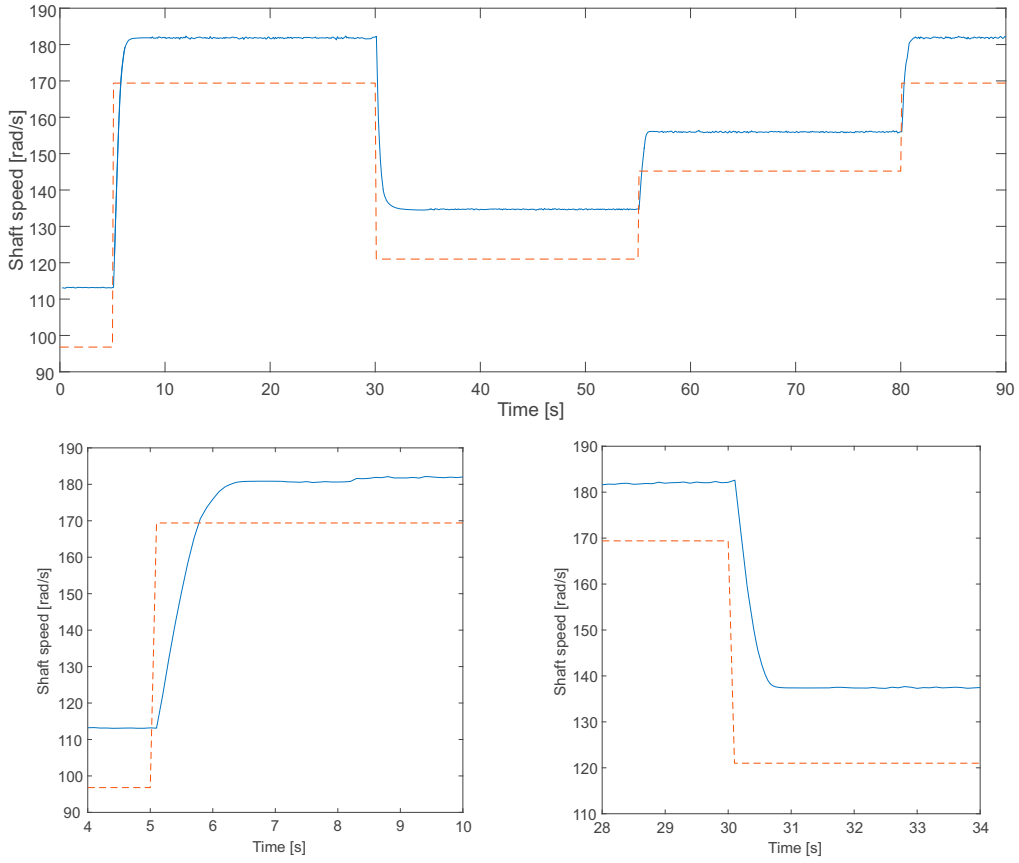

Figure 13. Optimal rotational speed reference for the variable wind profile (orange dashed line) and experimental speed tracking using only the FF controller (blue line).

To enrich the comparison analysis, the following experimental test presents the behavior of the system, adding a PI control term (PI + FF control in blue line in Figure 14). A two stages tuning procedure was used. Firstly, preliminary values for the PI's gains were computed using Ziegler–Nichols rules and, in a second tuning stage, those values were refined through simulation and experimental tests, obtaining the following gains: $k_p = 0.012$ and $k_i = 5$. It can be appreciated that the PI control action greatly improves the steady state offset error. However, the transient responses present overshoot, the first being the largest, of the order of 6%. In the zoomed view, it can also be observed a noticeable settling-time, of the order of 2 s.

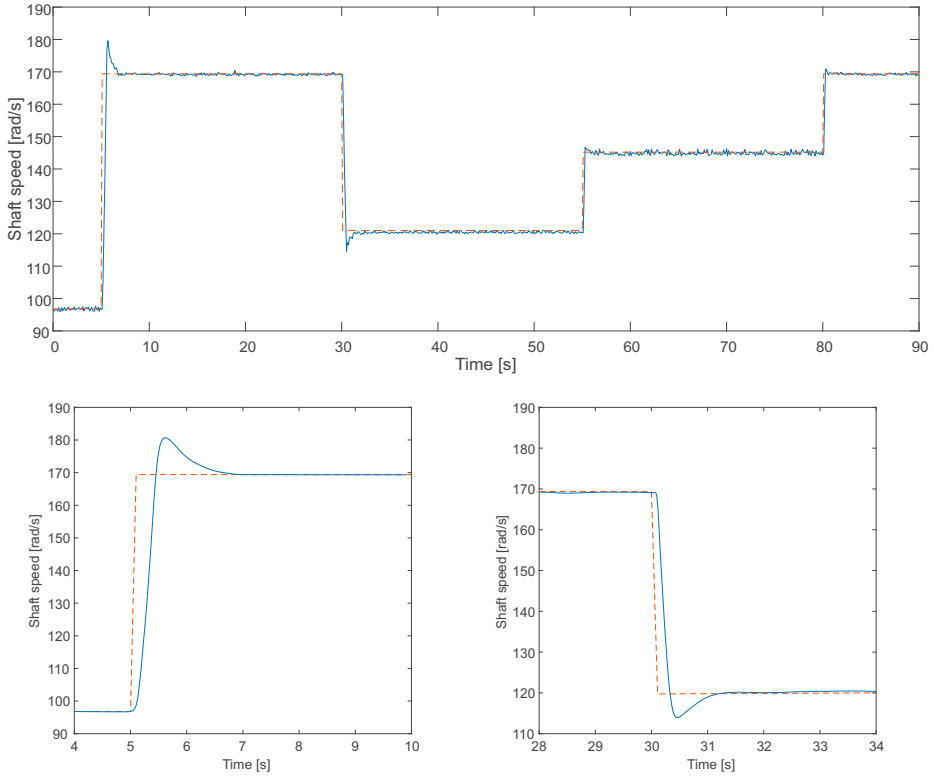

Figure 14. Optimal rotational speed reference for stepped wind profile (orange dashed line) and experimental speed tracking using the FF with a classic PI controller (blue line).

Finally, Figure 15 displays the experimental results obtained with the ST + FF control set-up. The proposed robust control strategy practically eliminates the steady state error, presents a negligible transient overshoot and very good settling-time (in less than 0.5 s the steady state is practically reached), achieving an excellent tracking of the optimal speed Ω_{opt}.

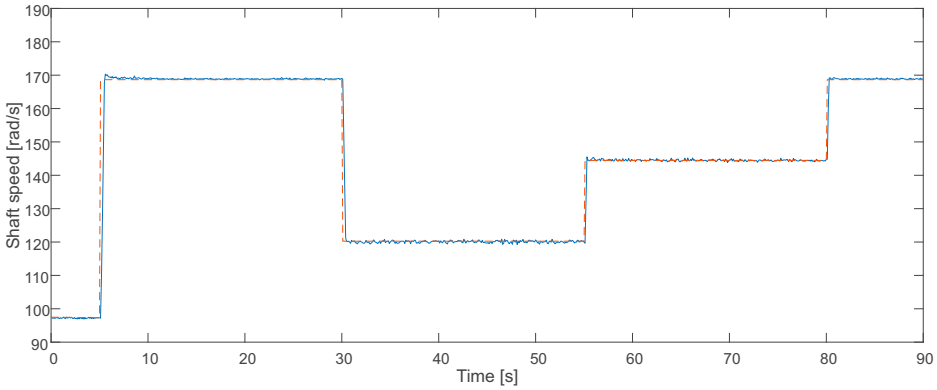

Figure 15. *Cont.*

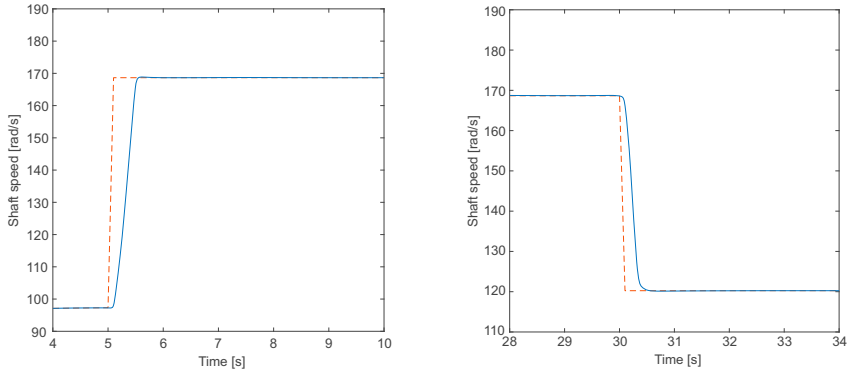

Figure 15. Optimal rotational speed reference for stepped wind profile and experimental speed tracking using the proposed ST + FF control set-up (overlapped).

5. Conclusions

Experimental results of the ST control set-up have been implemented and thoroughly assessed on a 5.5 kW WECS-DWIG laboratory test station, including comparison with a previous successful FF based control and with a classic PI controller. The proposed control strategy for this variable speed wind power generator proved to have excellent dynamic transient and steady-state performance.

The highly satisfactory results using the aforementioned approach confirmed the feasibility of the solution for implementation in real generation plants based on this type of generator. The principal advantages of the ST control set-up for a DWIG based wind turbine can be summarized as follows: guaranteed extended range of operation in spite of the nonlinear nature of the system; fast finite time convergence for MPPT; reduced mechanical stresses and chattering; robustness against real WECS parameter uncertainties/variations; on-line operation of the proposed controller not requiring of measured signals differentiation; and relatively simple controller structure, resulting in moderate real time computational burden.

As a future research line in this project, the encouraging results obtained with the proposed ST control set-up for the WECS-DWIG will lead to the development of a hybrid micro-grid (MG) topology. It will be designed to take advantage of the electrical features of the DWIG. The MG will present a DC bus, for generation and energy storage module interconnection, and an AC bus, for power exchange with a weak grid and the load. In addition to the main DWIG based wind power source, the MG will consider an ancillary power module (e.g., a photovoltaic module (PV)) and an energy storage module (ESM), with combined storage devices (high-power and high-energy density ones).

It is expected that this MG topology will unite the DWIG squirrel cage's robustness and its capacity to simultaneously generate to the DC and the AC buses, with the complementary capability of a storage module, resulting in a versatile MG.

Author Contributions: Conceptualization, P.F.P.; Formal analysis, J.I.T., P.F.P. and M.G.C.; Funding acquisition, J.A.B.-R. and P.F.P.; Investigation, J.I.T., P.F.P., M.G.C. and J.A.B.-R.; Methodology, P.F.P. and M.G.C.; Resources, J.A.B.-R.; Software, J.I.T.; Supervision, P.F.P.; Writing—original draft, M.G.C.; Writing—review & editing, J.I.T., P.F.P., M.G.C. and J.A.B.-R.

Funding: This research was funded by the Spanish Agencia Estatal de Investigación (AEI) and the Fondo Europeo de Desarrollo Regional (FEDER) under research projects DPI2015-67292-R (AEI/FEDER, UE) and the Argentinean projects ANPCyT PICT N2015-2257; UNLP 11/I217 and CONICET PIP 112-2015-0100496CO.

Acknowledgments: Many thanks to GAEI, DEEEA-ETSE, Universitat Rovira i Virgili (URV), Agencia Estatal de Investigación, from Spain, Fondo Europeo de Desarrollo Regional; and Universidad Nacional de La Plata (UNLP), Consejo Nacional de Investigaciones Científicas y Técnicas (CONICET), Agencia Nacional de Promoción Científica y Tecnológica (ANPCyT), Facultad de Ingeniería (FI-UNLP) and CIDEI, ITBA, from Argentina.

Conflicts of Interest: The authors declare no conflict of interest.

References

1. Bhutto, D.K.; Ansari, J.A.; Bukhari, S.H.; Chachar, F.A. Wind energy conversion systems (WECS) generators: A review. In Proceedings of the International Conference Computing, Mathematics and Engineering Technologies, Pakistan, Sukkur, Pakistan, 30–31 January 2019. [CrossRef]
2. Akinrinde, A.; Swanson, A.; Tiako, R. Dynamic Behavior of Wind Turbine Generator Configurations during Ferroresonant Conditions. *Energies* **2019**, *12*, 639. [CrossRef]
3. Basak, S.; Chakraborty, C. Dual stator winding induction machine: Problems, progress, and future scope. *IEEE Trans. Ind. Electron.* **2015**, *62*, 4641–4652. [CrossRef]
4. Muñoz, A.R.; Lipo, T.A. Dual stator winding induction machine drive. *IEEE Trans. Ind. Appl.* **2000**, *36*, 1369–1379. [CrossRef]
5. Bu, F.; Liu, H.; Huang, W.; Xu, H.; Hu, Y. Recent advances and developments in dual stator winding induction generator and system. *IEEE Trans. Energy Convers.* **2018**, *33*, 1431–1442. [CrossRef]
6. Amimeur, H.; Aouzellag, D.; Abdessemed, R.; Ghedamsi, K. Sliding mode control of a dual-stator induction generator for wind energy conversion systems. *Electr. Power Energy Syst.* **2012**, *42*, 60–70. [CrossRef]
7. Sarasola, I.; Poza, J.; Rodriguez, M.A.; Abad, G. Predictive direct torque control for brushless doubly fed machine with reduced torque ripple at constant switching frequency. In Proceedings of the IEEE International Symposium on Industrial Electronics (ISIE), Vigo, Spain, 4–7 June 2007; pp. 1074–1079.
8. Shao, S.; Abdi, E.; Barati, F.; McMahon, R. Stator-flux-oriented vector control for brushless doubly fed induction generator. *IEEE Trans. Ind. Electron.* **2009**, *56*, 4220–4228. [CrossRef]
9. Mahboub, M.A.; Drid, S.; Sid, M.A.; Cheikh, R. Sliding mode control of grid connected brushless doubly fed induction generator driven by wind turbine in variable speed. *Int. J. Syst. Assur. Eng. Manag.* **2017**, *8*, 788–798. [CrossRef]
10. Wu, Z.; Ojo, O.; Sastry, J. High-performance control of a dual stator winding DC power induction generator. *IEEE Trans. Ind. Appl.* **2007**, *43*, 582–592. [CrossRef]
11. Barrado-Rodrigo, J.A.; Talpone, J.I.; Martinez-Salamero, L. Variable-speed wind energy conversion system based on a dual stator-winding induction generator. *IET Renew. Power Gener.* **2017**, *11*, 73–80. [CrossRef]
12. Barrado-Rodrigo, J.A.; Valderrama-Blavi, H.; Ayad, M.; Talpone, J.I. Low-voltage ride through capability testing of a DWIG for wind power generation. In Proceedings of the IEEE International Conference on Compatibility, Power Electronics and Power Engineering, Cadiz, Spain, 4–6 April 2017. [CrossRef]
13. Utkin, V. Survey paper variable structure systems with sliding modes. *IEEE Trans. Autom. Control* **1977**, *22*, 212–222. [CrossRef]
14. Levant, A. Sliding order and sliding accuracy in sliding mode control. *Int. J. Control* **1993**, *58*, 1247–1263. [CrossRef]
15. Fridman, L.; Levant, A. Sliding mode control in engineering. In *Higher Order Sliding Modes*; Perruquetti, W., Barbot, J., Eds.; Marcel Dekker, Inc.: New York, NY, USA; Basel, Switzerland, 2002; Chapter 3; pp. 53–101.
16. Bartolini, G.; Pisano, A.; Punta, E.; Usai, E. A survey of applications of second-order sliding mode control to mechanical systems. *Int. J. Control* **2003**, *76*, 875–892. [CrossRef]
17. Fridman, L.; Moreno, J.; Iriarte, R. (Eds.) *Sliding Modes after the First Decade of the 21st Century*; Ser. Lecture Notes in Control and Information Sciences; Springer: Berlin/Heidelberg, Germany, 2012; Volume 412. [CrossRef]
18. Bandyopadhyay, B.; Janardhanan, S.; Spurgeon, S.K. (Eds.) *Advances in Sliding Mode Control. Concept, Theory and Implementation*; Ser. Lecture Notes in Control and Information Sciences; Springer: Heidelberg, Germany, 2013; Volume 440, p. 380. [CrossRef]
19. Fridman, L.; Barbot, J.-P.; Plestan, F. (Eds.) *Recent Trends in Sliding Mode Control*; IET: London, UK, 2016. [CrossRef]
20. Li, S.; Yu, X.; Fridman, L.; Man, Z.; Wang, X. (Eds.) *Advances in Variable Structure Systems and Sliding Mode Control Theory and Applications*; Ser. Studies in Systems, Decision and Control; Springer International Publishing: Cham, Switzerland, 2018; Volume 115. [CrossRef]
21. Shtessel, Y.; Edwards, C.; Fridman, L.; Levant, A. (Eds.) *Sliding Mode Control and Observation*; Springer: New York, NY, USA, 2013. [CrossRef]

22. Huangfu, Y.; Zhuo, S.; Rathore, A.K.; Breaz, E.; Nahid-Mobarakeh, B.; Gao, F. Super-twisting differentiator-based high order sliding mode voltage control design for DC-DC buck converters. *Energies* **2016**, *9*, 494. [CrossRef]
23. Beltran, B.; Benbouzid, M.; Ahmed-Ali, T. Second-order sliding mode control of a doubly fed induction generator driven wind turbine. *IEEE Trans. Energy Convers.* **2012**, *27*, 261–269. [CrossRef]
24. Martinez, M.I.; Susperregui, A.; Tapia, G. Second-order sliding-mode-based global control scheme for wind turbine-driven DFIGs subject to unbalanced and distorted grid voltage. *IET Electr. Power Appl.* **2017**, *11*, 1013–1022. [CrossRef]
25. Chavira, F.; Ortega-Cisneros, S.; Rivera, J. A Novel Sliding Mode Control Scheme for a PMSG-Based Variable Speed Wind Energy Conversion System. *Energies* **2017**, *10*, 1476. [CrossRef]
26. Benamor, A.; Benchouia, M.T.; Srairi, K.; Benbouzid, M. A novel rooted tree optimization apply in the high order sliding mode control using super-twisting algorithm based on DTC scheme for DFIG. *Int. J. Electr. Power Energy Syst.* **2019**, *108*, 293–302. [CrossRef]
27. Evangelista, C.A.; Pisano, A.; Puleston, P.; Usai, E. Receding-Horizon Adaptive Second-Order Sliding Mode Control for Doubly Fed Induction Generator Based Wind Turbines. *IEEE Trans. Control Syst. Technol.* **2017**, *25*, 73–84. [CrossRef]
28. Plestan, F.; Evangelista, C.; Puleston, P.; Guenoune, I. Control of a Twin Wind Turbines System without Wind Velocity Information. In Proceedings of the IEEE 15th International Workshop on Variable Structure Systems and Sliding Mode Control, VSS, Graz, Austria, 9–11 July 2018.
29. Bose, B.K. *Modern Power Electronics and AC Drives*; Prentice Hall: Upper Saddle River, NJ, USA, 2001.
30. Bartolini, G.; Ferrara, A.; Levant, A.; Usai, E. On second order sliding mode controllers. In *Variable Structure Systems, Sliding Mode and Nonlinear Control*; Young, K., Özgüner, Ü., Eds.; Lecture Notes in Control and Information Sciences; Springer: London, UK, 1999; Volume 247. [CrossRef]